Mesoscale and high-frequency variability of macroscopic particles (> 100 μm) in the Ross Sea and its relevance for late-season particulate carbon export

Alexander B. Bochdansky[*1], Melissa A. Clouse[1], Dennis A. Hansell[2]

[1] Ocean, Earth and Atmospheric Sciences, Old Dominion University, Norfolk, VA, USA

[2] Department of Ocean Sciences, University of Miami, Miami, FL, USA

[*]corresponding author. Email: abochdan@odu.edu

Abstract:

The Ross Sea plays a major role in the transfer of organic carbon from the surface into the deep sea due to the combination of high seasonal productivity and Antarctic bottom water formation. Here we present a particle inventory of the Ross Sea based on a combined deployment of a video particle profiler (VPP) and a high-resolution digital holographic microscope (DIHM). Long-distance (100s of kilometers) and short-distance (10s of kilometers) sections showed high variability of particle distributions that co-varied with the density structure of the water column. Particle export was apparent at sites of locally weakened pycnoclines, likely an indirect effect of nutrient (i.e., especially iron) mixing into the surface layer and local blooms that lead to export. Particle volume abundances at 200-300 m depth were highly correlated with particle volume abundances in the upper mixed layer (<60 m), consistent with particles at depth primarily the result of export rather than lateral advection. *Phaeocystis antarctica* (Haptophyta) colonies that were initially retained in the mixed layer sank below the euphotic zone within a period of two weeks. Fine-scale analysis at a resolution <1 m revealed a significantly overdispersed (i.e., highly patchy) environment in all casts. Patchiness, as determined by the Lloyd index of patchiness and the Index of Aggregation, increased in and below the pycnocline presumably due to aggregation of particles while accumulating on density gradients. In contrast, particles in the upper mixed layer and in the nepheloid layers were more randomly distributed. In 40 of the 84

VPP depth profiles, a periodicity of particle peaks ranged from 10 to 90 m with a mode of 30 m, which can be regarded as the "relevant scale" or "characteristic patch size" of the vertical distribution of particles. While chlorophyll fluorescence and particle mass determined by VPP were significantly correlated at higher particle abundances, the relationship changed from cast to cast, reflecting changes in the relative contribution of fresh phytoplankton to total particle mass. Particles that sank below the main pycnocline were composed of phytoplankton, marine snow with and without embedded phytoplankton, crustacean plankton, and a surprisingly high percentage of heterotrophic (and perhaps mixotrophic) protists, such as acantharians and tintinnids.

Keywords: marine snow, particulate flux, patchiness, spatial variations, vertical distribution, video particle profiler, digital holographic microscope, heterogeneity, mesoscale variability, phytoplankton, zooplankton, Ross Sea, Antarctica

1. Introduction

The nutrient-rich Ross Sea is the site of massive seasonal blooms of phytoplankton (primarily diatoms and *Phaeocystis antarctica*) and the accumulation of dissolved and particulate organic carbon (Carlson et al., 2000; DiTullio et al., 2010). Particle export in the Ross Sea has commonly been measured with sediment traps (e.g., Asper and Smith, 1999; Smith and Dunbar, 1998; Accornero et al., 1999), and the POC inventory of the water column has been measured on several expeditions using Niskin bottles and GF/F filters that capture particulate matter > ~0.7 μm (e.g., Carlson et al., 2000). However, particles between 50 μm to several millimeters contribute most to the mass flux, as smaller particles do not sink sufficiently fast and larger particles are too rare to play a major role as determined by Guidi et al. (2008) and McDonnell and Buesseler (2010). The smallest particles in this size range are primarily composed of single diatom cells ballasted by their silica skeletons (McDonnell and Buesseler, 2010). Surveys of these critical larger particles are rare, especially in the Ross Sea (Asper and Smith, 2003). Optical backscatter and beam transmissometry are responsive to fine particles and colloidal material (Battisto et al., 1999; Bochdansky et al., 2010), while large particles are more efficiently observed with camera systems (Stemmann et al., 2000; Guidi et al., 2008; Iversen et al., 2010).

In order to better understand the composition as well as the spatial and temporal distributions of macroscopic particles in the Ross Sea during the late season, we deployed a video particle profiler (VPP) in combination with a digital holographic microscope (DIHM).

2. Methods

2.1 Research expedition details

Data presented in this manuscript were collected on the RVIB *Nathaniel B Palmer* from February 12 to March 16, 2013 (cruise number NBP-1302). The main focus was on the western Ross Sea as it represents a significant site for Antarctic Bottom Water formation (Fig. 1). During this time period, the Ross Sea transitioned from being almost ice free to almost completely ice covered. We focused on three areas in the western Ross Sea: north of Franklin Island, south of Coulman Island, and Terra Nova Bay, each of which we revisited several times during the expedition in order to record temporal changes. Terra Nova Bay was the site of highest drawdown of inorganic carbon of all sites visited during this expedition (DeJong et al., 2015). We performed short-distance transects to obtain insight into the high-resolution spatial variability, and one long-distance zonal transect across the Ross Sea at the 76° 30'S line (Fig. 1), a section visited during many previous research cruises (e.g., Carlson et al., 2000; Smith et al., 2013). Casts used in this analysis (Fig. 1, Supplementary Table A1) are identified as those where either the VPP (dot) or the DIHM (triangle) or both (square) were deployed. The CTD with instruments was lowered at 0.5 m s^{-1} for the first 100 m, and then accelerated to 1 m s^{-1} for the remainder of each cast. Even at speeds of 1.5 m s^{-1}, our instrument yields sharp images (Bochdansky et al., 2013).

2.2 Video particle profiler (VPP)

The VPP was similar to that published in Bochdansky et al. (2010). However, instead of 45° angle lighting from both sides, side lighting with two white high-intensity LED lights was used ~7 cm in front of the lens. Some backscatter from transparent exopolymers (TEP), or from small particles embedded in that matrix, was possible using high intensity light. The light beams were

restricted using a slit width of 1 cm; however, as the light intensity dropped exponentially in the front and back of the image beam, only the brightest lit image plane was used for analysis. This method reduced bias caused by overlapping particles, removed motion blur streaks, and provided more accurate particle size estimates. At the focal plane, the field of view was 3.5 cm tall and 4.7 cm wide. The analysis program for the VPP was expanded from that in Bochdansky et al. (2010) to include more variables for particle characterization (including perimeter, volume and porosity). The VPP can record 30 images per second, with image analysis by a Linux-based image analysis program (an adapted Avidemux video editing software) at high speeds (approximately in real time after retrieval). The images were later aligned with depth from the CTD using time as the common variable and by filming a clock displaying UTC at the beginning and the end of each video sequence. In Matlab, CTD data were matched at one second resolution with the particle data. The raw data consisted of millions of particles with associated CTD data. These raw data allow us to resample particle metrics at all scales. Particle volumes were calculated as shown in Fig. 2. Instead of assuming a specific geometric shape, the projected area of the particle on the screen (sum of white and black pixels within the perimeter of the particle) was converted into a circle that was then converted to volume. This method reduces error in volume calculations greatly because 2-dimensional information rather than 1-dimensional information is used to reconstruct volumes, thus avoiding the bias of assigning disproportionally large volumes to elongated objects. This approach is widely used in image analysis of ocean particles (e.g., Iversen et al., 2010). Total particle volume (pixel^3 frame^{-1}) was approximated by multiplying the mean volume of particles with the mean particle number.

2.3 Digital inline holographic microscopy (DIHM)

Details of the DIHM were published in Bochdansky et al. (2013). Briefly, a laser beam is focused on a 9 μm single-mode optical fiber that serves as a small but intense point source of light. The expanding beam intercepts particles that create interfering shadow images on the adjacent screen of a high-resolution (4.2 megapixel) charge-coupled device (CCD) camera without lens. The camera was connected to an eBOX530-820-FL1.6G-RC computer (Axiomtek) with a Gb LAN cable; images were recorded on a 750 GB hard disk at a frame rate of ~7-12 images per second. When the laser beam intercepts a structure, a portion of the image beam

scatters and interferes with the light of the primary beam in a predictable pattern. This raw image represents a hologram that can then be reconstructed by applying the Kirchhoff–Helmholtz transform (Xu et al., 2001) in commercially available reconstruction software (Octopus, 4-Deep Inwater Imaging, formerly Resolution Optics). Being lens-less, the advantage of this method is that anything in the 7-cm long image beam can be reconstructed without having to adjust focus on the object. The entirety of the image beam volume (i.e., 1.8 ml in this configuration) can be reconstructed in this fashion, and thus explores orders of magnitude more volume than any lens-based system would at the same resolution. Reconstruction of the images and analysis (particle quantities, sizes and type) were performed manually as no reliable image reconstruction and analysis system currently exists for the DIHM. The DIHM is well suited to detect hard structures (e.g., silica, chitin, calcium carbonate, strontium sulfate) to a resolution as small as 5 μm, and reliably images particles of any composition from 50 μm to ~8 mm in the image volume (Bochdansky et al., 2013). The DIHM does not "see" TEP, which can only be inferred from the distribution of finer particles suspended in that matrix.

In the VPP, particle numbers cannot be directly assigned to a defined image volume because of the diffuse border of the unconstrained light beam and the fact that different particle types have different reflectivities. This is a common problem in particle analysis because ocean particles abound in gels that can only be partially visualized under intense light (Bochdansky et al., 2016). The gel phase represents a continuum between dissolved organic and particulate matter (Verdugo et al., 2004), and because gels are clear and do not scatter light well, particle number and size estimates dependent on the specific settings of the imaging system resulting in volume estimates that diverge by orders of magnitude depending on the optical system applied (Graham et al., 2012). Our system was trained on marine snow using high intensity light and visualizing as much of the mucous matrix as possible. Cross-calibration among existing imaging platforms will need to be performed in the future using standardized objects of relevant sizes and ranges of optical properties in order to determine absolute particle volume data. We therefore only provide relative particle volume (pixel^3 frame^{-1}) in this study. In contrast, the DIHM has a very precise image volume so the number of particles within the laser image beam can be enumerated and measured accurately.

The degree of overdispersion (i.e., patchiness) in the system was assessed using two indices. One, the Lloyd index of patchiness (Lloyd, 1967), is domain-dependent (i.e., zero values affect the estimates); the other one, the index of aggregation (Bez, 2000), is domain-independent.

The Lloyd index (Lloyd, 1967) was calculated as:

(equation 1) $$Lp = \left[m + \left(\frac{\sigma^2}{m} - 1\right)\right] m^{-1},$$

where *Lp* is the Lloyd index of patchiness, *m* the mean particle abundance (number of particles per frame in 1 m bins), and σ^2 the variance of the particle abundance.

The index of aggregation (Bez, 2000) was calculated as:

(equation 2) $$ia = \sum_i z_i^2 \, [S \times (\sum_i z_i)^2]^{-1},$$

where *ia* is the index of aggregation, z_i the particle density, and *S* the sample scale (set to 1 for this analysis).

2.4 Plankton identification using the DIHM

Because we were mostly interested in the composition of exported particles, we began our analysis at depths at and below the pycnocline, which ranged from 50 to ~ 200 m, depending on the cast. The configuration of the DIHM was intended to maximize image volume and to target particles deeper in the water column (i.e., those that contribute to export flux). This instrument is not suitable for surveys of the upper mixed layer (too many overlapping interference patterns) and a much smaller distance between light source and detector would have to be chosen. The sequence was run and stopped when a larger particle was encountered (approximately >20% of the screen). In this fashion all large particles (> 100 μm) were captured but also smaller particles that are closer to the point source of the laser beam. These smaller particles were eliminated from quantitative analysis during post-processing. Particle analysis continued until the end of the cast

or until image quality decreased as to hamper reconstruction (e.g., images became too bright to reconstruct because the light output of the laser increases at cold temperature). Ending depths ranged from 312 m to 721 m, with one cast ending at 1185m. The maximum length of each particle was determined using the measuring tool of the Octopus software, the same used for reconstructions. The lengths were further corrected using a calibration based on known object sizes. The 100 μm threshold corresponds well with the approximate minimum particle size as seen by the VPP. *Phaeocystis* colonies, because of their dense structure, did not reconstruct well (Fig. 3); however, they have a very characteristic shape and texture even in the unreconstructed holograms (Fig. 3) that we were able to verify in tests with laboratory cultures of *P. antarctica*. Consequently, we were able to perform a detailed analysis on *Phaeocystis* colonies on all casts through all depths (including the surface mixed layer).

Salinity, temperature, and oxygen measurements were obtained using SeaBird 911+ conductivity, temperature, and depth (CTD) probes. Salinity was calibrated on discrete samples at 24°C using a Guildline 8400 Autosal four-electrode salinometer. A Wetlabs ECO-FL fluorometer provided data on chlorophyll fluorescence.

All raw data from the VPP and the DIHM, including the CTD context data, were archived at BCO-DMO (http://www.bco-dmo.org/), cross-listed under the name of the principal investigator (Bochdansky) and the NSF research cruise number (NBP13-02).

The map and supplementary figure of *Phaeocystis* colony distribution were created using Ocean Data View (Schlitzer, 2015).

3. Results and Discussion

3.1 Long-distance transect at the 76° 30’ line with the VPP

Casts along the 76° 30’ line (total length > 500 km, Fig. 1) were taken over a period of 2.3 days (Fig. 4). Plotting the first derivative of potential density (referred to here as sigma theta' ($\sigma\Theta'$)) provided insights into the strength of the density discontinuities (Fig. 4a). Along this transect, the main pycnocline was weaker in some areas than others (arrows in Fig. 4a). At these sites, increased particle numbers were observed at depth and frequently appeared in bands (Fig. 4b). Layers of marine snow and thin layers of phytoplankton have frequently been observed to be associated with strong pycnoclines where particle maxima can be found in or just below the most pronounced density discontinuity (MacIntyre et al., 1995; Dekshenieks et al., 2001). Overall, the main pycnocline represented a strong separation with total particle volume concentrations in the upper mixed layer two orders of magnitude higher than below the pycnocline. Particle mass increased again at depth due to resuspension of benthic material (nepheloid layers in Fig 4b). Patchiness as indicated by the Lloyd index was highly variable throughout the water column, with the highest values generally found at casts and depths at which particle abundances were low; notable exceptions existed where high values coincided with particle peaks (Fig. 4c).

3.2 Short-distance transect south of Coulman Island with the VPP

Casts along this southwest- to northeast-oriented section (total length ~45 km, Fig. 1) were taken during a period of 3 days (Fig. 5). Similar to our observation in the long-distance transect and many other regions (not shown), increased particle numbers at depth (~200-300 m) were apparent where the pycnocline was locally weaker (arrows in Fig. 5a, Fig. 5b). Resuspension was also apparent above the benthos (Fig. 5b). As in the long zonal transect, the Lloyd index of patchiness generally corresponded inversely to total particle volume (with higher patchiness at lower particle numbers), but also showed high values within or just below the pycnocline where large aggregates were typically present (Fig. 5c).

3.3 Relationship between water column stability and particle export

We tested the hypothesis whether the density structure of the water column influences particle abundances by combining all VPP data from this expedition. To this end we regressed total particle volumes in the 200 to 300 m depth range against the maximum values of sigma theta' within the first 150 m (as indicator of the strength of the pycnocline). Indeed the slope was significantly different from zero and negative (Fig. 6a). This inverse relationship could be partially explained by the fact that particles would more easily sink where stratification of the water column is locally weakened and some mixing occurs (Ruiz et al. 2004). However, particle volumes in the upper 60 m (in the mixed layer) were even more highly correlated with the maximum sigma theta', with ~ 23% of the variance explained (Fig. 6b). This latter observation suggests that local mixing supplies nutrients to the upper mixed layer and that the increased particle abundance is a result of that. Finally, particle volume abundances in the mixed layer (< 60 m) and at depths below the pycnocline (200-300 m) were highly positively correlated with a high percentage of explained variance (56%, Fig. 6c). Because of this close relationship between particle inventories at the surface and at depth, we conclude that particles observed at depth are indeed exported from the surface waters, and not merely the result of lateral advection from adjacent continental slopes. A connection between nutrient inputs and large aggregate formation has previously been made for open ocean systems (between the Azores and the Iberian peninsula, Guidi et al., 2007). Also, aggregation and sinking can occur over surprisingly short times scales (e.g., Lampitt et al., 1993; Jouandet et al., 2014; Jackson et al., 2015). Because macronutrients are replete in the Ross Sea over the entire season, iron is the most likely nutrient to stimulate these local late season blooms (Sedwick et al., 2000). Dissolved iron fluxes have been reported from deeper water (benthic sources > 400 m, Marsay et al., 2014; McGillicuddy et al., 2015), some circumpolar deep water intrusions (Gerringa et al., 2015), and horizontal transport from the landmasses and slopes may also be factors (Gerringa et al., 2015). Ice melt is not a source of iron in the austral fall (McGillicuddy et al., 2015), the time of our observations.

The lack of a suitable calibration (see Methods) prevents these particle number and volumes from being directly compared to earlier optical surveys of Ross Sea particles > 500 μm (Asper and Smith, 2003). However, it is important to note that total particle volumes in our study ranged approximately over three orders of magnitude (Fig 4b, 5b, 6a). When multiplying the extremes

of the ranges in mean particle size (0.8-1.7 mm) with the extremes of ranges in mean particle abundances (~1 to 230) in the study by Asper and Smith (2003), and assuming sphericity for particles, the total ranges in volume concentrations were 0.27 to 591 mm^3 L^{-1}. The resulting factor of 2,189 x is thus consistent with our result of three orders of magnitude ranges in volume concentrations.

3.4 Fine-scale distribution

High-resolution and high-frequency analyses of particles by the VPP allowed us to explore vertical patchiness on a meter-scale. These small scales are relevant for plankton dynamics and biophysical processes (Wolk et al., 2004). Our analysis was based on individual frames collected at a frame rate of 30 per second, each of which surveys approximately 4 ml of seawater. These data were averaged over meter bins, which was consequently the smallest spatial scale of this analysis. Whether or not particle distributions at this scale were significantly overdispersed was tested by comparing the frequency distribution of particle counts with a standard Poisson distribution. Particle distributions were significantly overdispersed ($p<0.005$) in all profiles at these small scales, especially below the pycnocline and above the nepheloid layer.

The two indices (the index of aggregation (*ia*) and the Lloyd index of patchiness (*Lp*)) showed similar trends, but they were also markedly different from each other (Fig. 7). Sometimes the relationship bifurcates: the *ia* seems to flatten (no response to higher degree of overdispersion) where the *Lp* shows large deviations at higher values (Fig. 7). We conclude that the Lloyd index is a better metric in describing highly overdispersed micropatches. A Lloyd index of 1 (i.e., variance = mean) reflects a random distribution of particles as was the case in the presence of finely suspended material such as found in the upper mixed layer and in the bottom nepheloid layer (Fig. 4 and 5). Particle distributions that are more evenly (i.e., uniformly) distributed (i.e., variance < mean) would have a value of <1. When subsampling the same data over increasingly larger spatial scales (1 m, 3 m, 5 m, 11 m, etc.), the Lloyd index of patchiness quickly approached values close to one, indicating a more random distribution of particles at these larger scales (not shown).

Arbitrary binning into larger and larger depth intervals, however, misses the periodicity that was apparent in the particle peaks through the water column. For this reason, we tested for periodicity using fast Fourier transforms (FFT) for each cast. Of 84 casts, almost half (n = 40) showed a clear peak in the periodogram (example in Fig. 8b). Casts that did not show periodicity of smaller particle peaks often displayed one or two very prominent peaks (Fig. 8c). For casts with detectable periodicities, average peak-to-peak distances ranged from 10 to 90 m, with the most frequent bin being 30 m (Fig. 9). These periodicities can be interpreted as the "characteristic patch size" for particle peaks. Given the relevance of a continuum of temporal and spatial scales to phytoplankton growth (Harris, 1980), even small observed periodicities require overwhelming physical or biological forcing mechanisms. In other words, even subtle observed frequencies may indicate very strong causes. While intriguing, it is unclear what caused the observed periodicity in particle peaks. These peaks can be the result of water column density structure (i.e., particle settling being slowed at local pycnoclines), episodic sinking events, or both. Smith et al. (2011) observed high temporal variability of fluorescence in surface water that they attributed to wind-induced advective changes. It is thus possible that periodicity in weather patterns would lead to the observed periodicities in particle peaks with depth. This forcing would be in addition to factors known to control export, such as surface production and grazer community composition (Smith and Dunbar, 1998). The vastly different particle profiles in casts 52 and 53, which were only 5 hours and 31 km apart, highlights the high mesoscale variability of this region (Fig. 8a.c).

The relationship between particle volume abundance and the relative fluorescence was investigated in an attempt to reveal changes in the quality of the flux. Fluorescence and particle volume abundance were correlated albeit at low r^2 values and only at a relative fluorescence > 0.1 (Fig. 10). Below a relative fluorescence of 0.1, no relationship to particle volume abundance was apparent (Fig. 10). In some casts, the ppm and fluorescence data were more tightly coupled (Fig. 10a), while in other casts the variables diverged widely (Fig. 10b). A relatively tight coupling between fluorescence and total particle volume may be indicative of fresh phytoplankton dominating overall particle mass. One location that was probed within 2 weeks

(casts 55 and 104) not only revealed a more variable relationship between total particle volume and fluorescence but also displayed significant differences in slopes and elevations of the regression lines over the two week interval (for fluorescence > 0.1: ANCOVA, n = 360, homogeneity of slopes: $F = 81.03$, $p \ll 0.0001$; elevation: $F = 365.0$, $p \ll 0.0001$, Fig. 10 b). Changes in the relationship between fluorescence and the total particle volume as detected by video images may thus be a useful indicator for the relative state of degradation of particulate matter, assuming that fresh phytoplankton material at the surface would have the highest fluorescence relative to particle volume, while particles dominated by heterotrophs, marine snow mucous matrix, and more refractory phytoplankton would show lower fluorescence-to-particle volume ratios. However, poor correlation between particle volume and fluorescence have also been attributed to the presence of large zooplankton and the formation of large aggregates in deeper layers containing fewer phytoplankton cells (Petrik et al., 2013).

3.5 Particle composition and plankton distributions from the DIHM

We examined the composition of large particles using the DIHM for 26 casts. The number of particles classified ranged from 14 to 523 with an average number per cast of 124. In total, 3721 particles were analyzed. The particles were grouped into four categories: marine snow, phytoplankton, zooplankton, and “others” (Fig. 11 and 12). “Others” included particles clearly organismal but that could not be classified with certainty, and optically dense singular particles that did not classify as marine snow or organismal, some of which may have been large fecal pellets.

Despite high variability in the number of particles found during each cast, relative particle composition was relatively consistent, either being dominated by marine snow, phytoplankton, or co-dominated by both. Marine snow included amorphous aggregates, clusters, stringers, and aggregates containing organisms (Fig. 12). Phytoplankton included *Rhizosolenia* spp. (30% of total phytoplankton observed), *Corethron* spp. (7%), *Chaetoceros* spp. (0.2%), other diatoms, and dinoflagellates (0.1%) (Fig. 12). Analysis of *Phaeocystis* colonies was performed separately and in more detail (see below). Phytoplankton below the main pycnocline can be regarded as

exported as they are not able to return to the sunlit surface waters. Intact phytoplankton have routinely been found at even greater depths than in the Ross Sea (Agusti et al., 2015 and references cited therein). Zooplankton at depth included acantharians (52% of total zooplankton observed), copepods (24%), tintinnids (9%), larvaceans (7%), and nauplii (5%) (Fig. 12). Acantharians were widespread, being found in the majority of the casts.

As expected, many of the larger particles were composed of marine snow that were either amorphous with unidentifiable content, or contained large numbers of aggregated diatoms (Fig. 11 and 12). Particles below the main pycnocline were composed of a surprisingly large number of zooplankton, and because they cannot migrate back into the mixed surface layer (except for the largest copepods), were either exported or normally reside at these depths. The paucity of prey at these depths makes export from the surface more likely. Acantharians, ciliates, radiolarians, and foraminifera are known for kleptoplasty (Stoecker et al., 2009), therefore there is some overlap in the zooplankton and phytoplankton categories. Among ciliates, only loricate forms image well with the DIHM, which means that the total ciliate numbers would have to be ~10 times higher when accounting for the much more numerous aloricate ciliates (Assmy et al., 2013 PNAS supplementary section, Fig. 53 therein). The lack of radiolaria and foraminifera in our samples was remarkable given that they should produce good images with the DIHM. This result means that among Cercozoa (including former Radiolaria) and Retaria (including Foraminifera and Acantharia; Adl et al., 2005), Acantharia were the most abundant. These organisms were historically underestimated as they are lost with conventional preservation methods (Beers and Stewart, 1970).

3.6 *Phaeocystis antarctica* colony distribution

Phaeocystis antarctica colonies were remarkably confined to a region between 169° and 190°E (Supplementary Fig. A1). This distribution corresponds well with the highest abundances observed by DiTullio et al. (2010) for earlier parts of the seasonal growth cycle. Abundances were highest at cast 15 (a station further north of the 76° 30’S line), followed by cast 121 (Fig. 1, supplementary Fig. A1), both in terms of average numbers of *Phaeocystis* colonies and as

integrated stock over the entirety of the mixed layer (data not shown). Over our observation period of two weeks, we observed sinking of a large number of colonies from the surface mixed layer, through the pycnocline, and into the deeper layer (i.e., *Phaeocystis* colonies have undergone export). This penetration of *Phaeocystis* into deep water was associated with a weakening of the pycnocline during the same period (Fig. 13). Thus *Phaeocystis* colonies not only contribute significantly to total export production during the main growing season in the austral spring and summer (DiTullio et al., 2010) but also in the fall. Our observations, showing retention on strong pycnoclines followed by significant export, is consistent with previous sediment trap observations (Smith and Dunbar, 1998).

4. Conclusions

Spatial and temporal variability of particles >100 µm is very high in the autumnal Ross Sea at all measured scales. We observed a characteristic banding pattern in the microscale distribution of particles at characteristic scales of tens of meters. These finer bands may reflect sinking events as a result of cyclical wind events that locally erode the main pycnocline. But these bands may also be the result of fine-scale changes in the density structure of the water column that allow particles to accumulate. On a larger scale, we found that particle abundances over larger depth ranges (0-60 m, 200-300 m) corresponded with weaker pycnoclines, which may reflect enhanced vertical mixing that bring nutrients (particularly iron) to the surface and promote local blooms. The high correlation between particle volume abundances between the surface and the deep strongly suggests local export at these sites. Analysis of DIHM images revealed that particles below the main pycnocline have a large contribution of live or moribund plankton, which represent a source of relatively undegraded carbon for deeper layers. This process is also reflected in the relatively loose correlation between fluorescence and total particle volume, partly because of the limit of detection by the fluorometer, but also because the relationship between total particle volume and fluorescence changes both temporally and with depth.

Acknowledgements: We thank our co-PIs on this project Robert Dunbar, Jack DiTullio, and Monica Orellana. Cody Garrison helped with the deployment of the DIHM and the VPP. Martin Laan (Royal Netherlands Institute of Sea Research) greatly improved the electronics of the DIHM. We also thank the crew of the RVIB *Nathaniel B Palmer* and the Lockheed Martin Antarctic Support Contract team. This project was funded by the National Science Foundation, Division of Polar Program grants #1142097 to ABB and # 1142117 to DAH.

References

Accornero, A., Bergamasco, A., Monaco, A., Tucci, S., 1999. Particle fluxes at the edge of the Ross Ice Shelf: the role of physical forcing. Oceanography of the Ross Sea Antarctica, eds Spezie G, Manzella GMR (Springer, Milan), pp 177-195.

Adl, S.M., Simpson, A.G.B., Farmer, M.A. et al. 2005. The new higher level classification of eukaryotes with emphasis on the taxonomy of protists. J. Eukaryot. Microbiol. 52(5), 399-451.

Agusti, S., Gonzalez-Gordillo, J.I., Vaque, D. et al. 2015. Ubiquitous healthy diatoms in the deep sea confirm deep carbon injection by the biological pump. Nature Comm. 6, 7608.

Asper, V.L., Smith Jr, W.O., 1999. Particle flux during austral spring and summer in the southern Ross Sea, Antarctica. J. Geophys. Res. 104, C3, 5345-5359.

Asper, V.L., Smith Jr, W.O., 2003. Abundance, distribution and sinking rates of aggregates in the Ross Sea, Antarctica. Deep-Sea Res. I, 50, 131-150.

Assmy, P., Smetacek, V., Montresor, M., et al. 2013. Thick-shelled, grazer-protected diatoms decouple ocean carbon and silicon cycles in the iron-limited Antarctic Circumpolar Current. PNAS. 110(51), 20633-20638.

Battisto, G.M., Friedrichs, C.T., Miller, H.C., Resio, D.T., 1999. Response of OBS to mixed grain size suspensions during SandyDuck ’97. Coastal Sediments: Proceedings of the International Symposium on Coastal Engineering and Science of Coastal Sediment Processes, eds Kraus NC, McDougal WG (Hauppauge, Long Island, New York), pp 297–312.

Beers, J.R., Stewart, G.L., 1970. The preservation of acantharians in fixed plankton samples. Limnol. Oceanogr. 15(5), 825-827.

Bez, N., 2000. On the use of Lloyd’s index of patchiness. Fish. Oceanogr. 9(4), 372-376.

Bochdansky, A.B.B., Clouse, M.A., Herndl, G.J., 2016. Dragon kings of the deep sea: marine particles deviate markedly from the common number-size spectrum. Sci. Rep. 6, 22633.

Bochdansky, A.B.B., Jericho, M.H., Herndl, G.J., 2013. Development and deployment of a point-source digital inline holographic microscope for the study of plankton and particles to a depth of 6000m. Limnol. Oceanogr. Methods. 11, 28-40.

Bochdansky, A.B.B., van Aken, H.M., Herndl, G.J., 2010. Role of macroscopic particles in deep-sea oxygen consumption. PNAS. 107(18), 8287-8291.

Carlson, C.A., Hansell, D.A., Peltzer, E.T., Smith Jr, W.O., 2000. Stocks and dynamics of dissolved and particulate organic matter in the southern Ross Sea, Antarctica. Deep-Sea Res. II 47, 3201-3225.

DeJong, H.B., Dunbar, R.B., Mucciarone, D., Koweek, D.A., 2015. Carbonate saturation state of surface waters in the Ross Sea and Southern Ocean: controls and implications for the onset of aragonite undersaturation. Biogeosciences 12, 6881-6896.

Dekshenieks, M.M., Donaghey, P.L., Sullivan, J.M. et al. 2001. Temporal and spatial occurrence of thin phytoplankton layers in relation to physical processes. Mar. Ecol. Prog. Ser. 223, 61-71.

DiTullio, G.R., Grebmeier, J.M., Arrigo, K.R. et al. 2010. Rapid and early export of *Phaeocystis antarctica* blooms in the Ross Sea, Antarctica. Nature 404, 595-598.

Gerringa, L.J.A., Lann, P., van Dijken, G.L. et al. 2015. Sources of iron in the Ross Sea in early summer. Mar. Chem. 177, 447-459.

Graham, G.W., Davies, E.J., Nimmo-Smith, Q.A.M. et al. 2012. Interpreting LISST-100X measurements of particles with complex stage using digital in-line holography. J. Geophys. Res. 117, C05034.

Guidi, L., Jackson, G.A., Stemmann, L. et al. 2008. Relationship between particle size distribution and flux in the mesopelagic zone. Deep-Sea Res. 1. 55, 1364-1374.

Guidi, L., Stemmann, L., Legendre, L. et al. 2007. Vertical distribution of aggregates (>110 um) and mesoscale activity in the northeastern Atlantic: Effects on the deep vertical export of surface carbon. Limnol. Oceanogr. 52(1), 7-18.

Harris, G.P., 1980. Temporal and spatial scales in phytoplankton ecology. Mechanisms, methods, models, and management. Can. J. Fish. Aquat. Sci. 37, 877-901.

Iversen, M.H., Nowald, N., Ploug, H., Jackson, G.A., Fischer G., 2010. High resolution profiles of vertical particulate organic matter export off Cape Blanc, Mauritania: Degradation processes and ballasting effects. Deep-Sea Res. 1. 57, 771-784.

Jackson, G.A., Checkly Jr, D.M., Dagg, M., 2015. Settling of particles in the upper 100m of the ocean detected with autonomous profiling floats off California. Deep-Sea Res. I 99, 75-86.

Jouandet, M.P., Jackson, G.A., Carlotti, F. et al. 2014. Rapid formation of large aggregates during the spring bloom of Kerguelen Island: observations and model comparisons. Biogeosciences. 11, 4393-4406.

Lampitt, R.S., Hillier, W.R., Challenor, P.G., 1993. Seasonal and diel variation in the open ocean concentration of marine snow aggregates. Nature 362, 737-739.

Lloyd, M., 1967. Mean crowding. J. Anim. Ecol. 36, 1-30.

MacIntyre, S., Alldredge, A.L., Gotschalk, C.C., 1995. Accumulation of marine snow at density discontinuities in the water column. Limnol. Oceanogr. 40(3), 449-468.

Marsay, C.M., Sedwick, P.N., Dinniman, M.S. et al. 2014. Estimating the benthic flux of dissolved iron on the Ross Sea continental shelf. Geophys. Res. Lett. 41, doi:10.1002/2014GL061684.

Mathot, S., Smith Jr, W.O., Carlson, C.A. et al. 2000. Carbon partitioning within *Phaeocystis antarctica* (Prymnesiophyceae) colonies in the Ross Sea. J. Phycol. 36, 1049-1056.

McDonnell, A.M.P., Buesseler, K.O., 2010. Variability in the average sinking velocity of marine particles. Limnol. Oceanogr. 55(5), 2085-2096.

McGillicuddy Jr, D.J., Sedwick, P.N., Dinniman, M.S. et al. 2015. Iron supply and demand in an Antarctic shelf ecosystem. Geophys. Res. Lett. 42, doi:10.1002/2015GL065727.Schlitzer, R., 2015. Ocean Data View, http://odv.awi.de.

Petrik, C.M., Jackson, G.A., Checkley Jr., D.M. 2013. Aggregates and their distributions determined from LOPC observations made using an autonomous profiling float. Deep-Sea Res. I, 64-81.

Ruiz, J., Macias, D., Peters, F. 2004. Turbulence increases the average settling velocity of phytoplankton cells. PNAS 101, 17720-17724.

Sedwick, P.N., DiTullio, G.R., Mackey, D.J. 2000. Iron and manganese in the Ross Sea, Antarctica: Seasonal iron limitation in Antarctic shelf waters, J. Geophys. Res., 105(C5), 11,321–11,336, doi:10.1029/2000JC000256

Smith Jr, W.O., Asper, V., Tozzi. S. et al. 2011. Surface layer variability in the Ross Sea, Antarctica as assessed by in situ fluorescence measurements. Prog. Oceanogr. 88, 28-45.

Smith Jr, W.O., Dunbar, R.B., 1998. The relationship between new production and vertical flux on the Ross Sea continental shelf. J. Mar. Sys. 17, 445-457.

Smith Jr, W.O., Tozzi, S., Long, M.C. et al. 2013. Spatial and temporal variations in variable fluorescence in the Ross Sea (Antarctica): Oceanographic correlates and bloom dynamics. Deep-Sea Res. I. 79, 141-155.

Stemmann, L., Picheral, M., Gorsky, G., 2000. Diel variation in the vertical distribution of particulate matter (>0.15 mm) in the NW Mediterranean Sea investigated with the Underwater Video Profiler. Deep-Sea Res. 1. 47, 505-531.

Stoecker, D. K., Johnson, M. D., De Vargas C., Not F. (2009). Acquired phototrophy in aquatic protists. Aquat. Microb. Ecol. 57, 279–310.

Wolk, F., Seuront, L., Yamazaki, H. et al. 2004. Comparison of biological scale resolution from CTD and microstructure measurements. In: Handbook of Scaling Methods in Aquatic Ecology: Measurement, Analysis, Simulation, Seuront L et al (ed), 3-15.

Verdugo, P., Alldredge, A.L., Azam, F. et al. 2004. The oceanic gel phase: a bridge in the DOM-POM continuum. Mar. Chem. 92, 67-85.

Xu, W., Jericho, M.H., Meinertzhagen, I.A. et al. 2001. Digital in-line holography for biological applications. PNAS. 98(20), 11301-11305.

Figure legends:

Fig. 1. Locations of casts at which the VPP and the DIHM were deployed during the TRACERS research expedition, February 12 to March 16, 2013. Symbols: VPP only (dots), DIHM only (triangles), and both VPP and DIHM (squares) were successfully deployed. The positions of the short and long transects are indicated by red lines. Casts specifically mentioned in the text and in the figures are labeled. Supplementary figure A1 includes cast 15 in the transect that had the highest *Phaeocystis* colony numbers during the entire expedition.

Fig. 2. Method for approximating particle volumes. Image analysis determines the projectional area of an irregularly shaped particle. On the basis of this area, the equivalent spherical diameter is calculated based on a circle with the same area, which in turn determines the volume of a sphere of the same diameter. The advantage of this method is that elongation and irregularities of objects are accounted for in volume calculations (Iversen et al., 2010).

Fig. 3. Four *Phaeocystis antarctica* colonies in a single unreconstructed hologram (a), and after reconstruction of one colony (b). The image volume of an individual hologram is 1.8 ml, but the reconstruction can only visualize a specific image plane within that volume. We concluded that *Phaeocystis* colonies were sufficiently distinguishable and unique that unreconstructed images could be used for quantification. Poor reconstruction of *Phaeocystis* colonies makes exact size determination unreliable but colony diameters in field collections in the Ross Sea range from approximately 10 to 400 μm (Mathot et al., 2000).

Fig. 4. Long-distance transect along the 76° 30’S line (distance given from west to east, Fig. 1). Black line (Fig. 1) indicates location and depth ranges of the casts. Variables from top to bottom are: (a) the first derivative of sigma theta' (σΘ') in 25 m bins, indicating the strength of the pycnocline; (b) the total particle volume (pixel^3 frame^{-1}) as the product of mean particle abundances and mean particle volume in the VPP casts; (c) the Lloyd index of patchiness calculated according to equation 1 (at a random distribution of particles Lloyd index = 1).

Increase of particle concentration near the bottom is due to a pronounced nepheloid layer. Arrows indicate weaker main pycnoclines concomitant with bands of exported particles at depth.

Fig. 5. Short-distance section south of Coulman Island (from southwest to northeast, Fig. 1). Black line (Fig. 1) indicates the location and depth ranges of the casts. Variables from top to bottom are: (a) the first derivative of sigma theta (σΘ') in 25 m bins indicating the strength of the pycnocline; (b) the total particle volume (pixel^3 frame^{-1}) as the product of mean particle abundances and mean particle volume at each meter of depth based on the VPP casts; (c) the Lloyd index of patchiness calculated according to equation 1 (at a random distribution of particles L_p = 1). Particle volume abundances are increased near the bottom due to a pronounced nepheloid layer. Arrows indicate weaker main pycnoclines concomitant with bands of exported particles at depth.

Fig. 6. (a) Total particle volume concentrations at depth (200 – 300 m) in relation to the strength of the pycnocline. (b) Total particle volume concentrations in the upper mixed layer in relation to the strength of the main pycnocline (defined as the maximum of the first derivative of sigma theta in the top 150 m, σΘ'). (c) Relationship between total particle volume concentration at 200 – 300 m and those in the surface mixed layer (< 60 m) for all VPP casts combined. Regression equations are (a) $y = 2.733 - 3.219\,x$, $n = 77$, $r^2 = 0.084$, $F = 6.90$, $p = 0.0105$; (b) $y = 4.395 - 8.532$, $F = 23.33$, $n = 78$, $r^2 = 0.235$, $p<0.0001$; (c) $y = 0.914 - 0.417\,x$, $n = 77$, $r^2 = 0.475$, $F = 67.92$, $p<0.0001$. Residuals failed normality thus p-values were generated using randomizations (10,000 x) of the data to produce custom F-distributions for each set.

Fig. 7. Three representative examples of the relationship between the Index of Aggregation (Bez, 2000) and the Lloyd index of patchiness (Lloyd, 1967) at submeter scales (~ 3.3 cm) from the VPP. A Lloyd index of 1 means that particles are randomly distributed, which most frequently occurred in the surface mixed layer. In some casts a bifurcation of the two indices was apparent

(a). At higher levels of overdispersion, the Lloyd index shows a stronger numerical response than the Index of Aggregation, which means it is more useful at higher levels of patchiness.

Fig. 8. Depth distribution of particle numbers (mean number of particles per frame in meter bins) versus depth (m) from the VPP. The inserts show the periodogram power spectral densities against vertical distance (i.e., depth ranges) after fast Fourier transformation. (a) Example with no periodicity. (b) The most frequently encountered case (40 of 84 casts), in which a periodicity was detectable at depth intervals shown in Fig. 9. (c) A large subsurface particle peak in some casts masked possible underlying periodicities at higher frequencies.

Fig. 9. Frequency distribution of peak periodicity of all casts in the VPP (n=40) that had a detectable higher frequency in the particle distribution through the water column. In one fourth of the peaks in the FFT periodogram (i.e., the basic modulus-squared of the discrete Fourier transform, n=10), the peak fell in the 30 m depth bin. This means that particle peaks occurred repeatedly at ~30 m depth intervals in the water column.

Fig. 10. Total particle volume concentration (relative numbers) versus fluorescence (relative fluorescence units) at two locations in the western Ross Sea and at two points in time (black vs white symbols) from the VPP. (a) Good agreement between total particle volume and fluorescence indicating that fresh phytoplankton dominate the flux. Regression equations (on log-transformed values) were only applied for relative fluorescence > 0.1: Cast 28 (black): $y = 3.37 + 0.70x$, $n = 174$, $r^2 = 0.86$; Cast 101 (white): $y=3.30+0.66x$, $n=202$, $r^2=0.80$. (b) The relationship between total particle volume and fluorescence varied greatly over a period of 2 weeks. Cast 55 (black): $y=3.73+1.12x$, $n=189$, $r^2=0.88$; Cast 104 (white): $y=3.03+0.63x$, $n=174$, $r^2=0.55$.

Fig. 11. Examples of DIHM images from our analysis. Images were cropped. Measurements of longest axis length are included in parentheses. (a-c) stringer-type marine snow particles (1322.87 μm, 1422.12 μm, 645.23 μm), (d-e) amorphous marine snow particles held together by optically TEP (1821.49 μm, 628.95 μm), (f-g) diatoms embedded in marine snow (536.74 μm, 1346.72 μm), (h) *Corethron* spp. (492.25 μm), (i-j) chain forming diatoms (563.66 μm, 463.65 μm), (k) *Rhizosolenia* sp. (422.27 μm), (l-m) acantharians (623.54 μm, 867.22 μm), (n-o) tintinnids (448.91 μm, 1729.85 μm), (p) copepod (421.89 μm), (q) *Fritillaria* sp. (824.68 μm), (r) nauplius (326.14 μm), (s) crustacean carcass (509.17 μm), (t) krill fecal pellet (451.97μm).

Fig. 12. Pie charts of the relative contribution of various particle groups (marine snow, phytoplankton, zooplankton, others) to total particle numbers below the pycnocline from the DIHM. We consider these particles as exported or resident species as only the largest zooplankton (too rare to be accounted for by the DIHM) would be able to swim back into the upper mixed layer. The "others" category included unidentified organisms as well as single optically dense particles that were neither marine snow nor organismal.

Fig. 13 Vertical distribution of *Phaeocystis antarctica* colonies (numbers liter^{-1}) in relation to sigmaΘ. *Phaeocystis antarctica* colonies reached much deeper when the density gradients partially eroded (c and d) approximately 2 weeks later. Lines represent sigma theta' (σΘ) and 15-m moving averages (ma). (a) Cast 9, (b), Cast 15, (c) Cast 124, (d) Cast 127 (Fig. 1).

Figure 1
Click here to download high resolution image

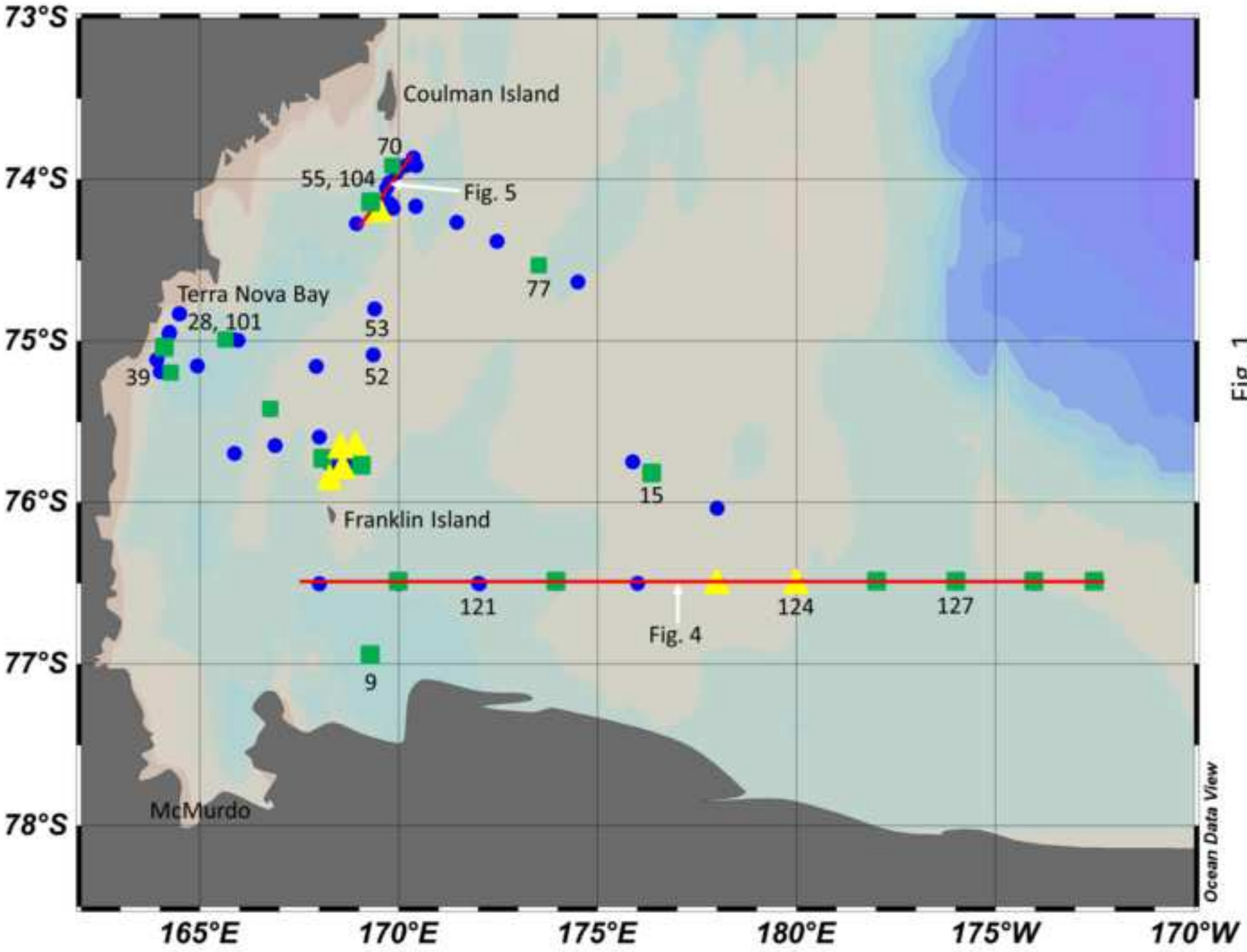

Fig. 1

Figure 2
Click here to download high resolution image

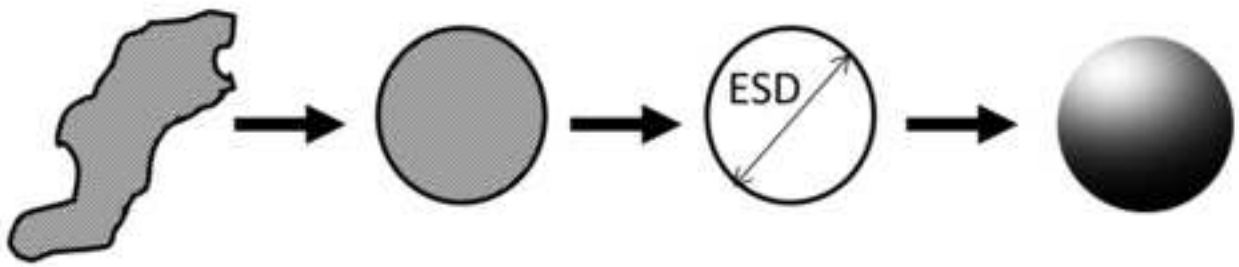

Fig. 2

Figure 3
Click here to download high resolution image

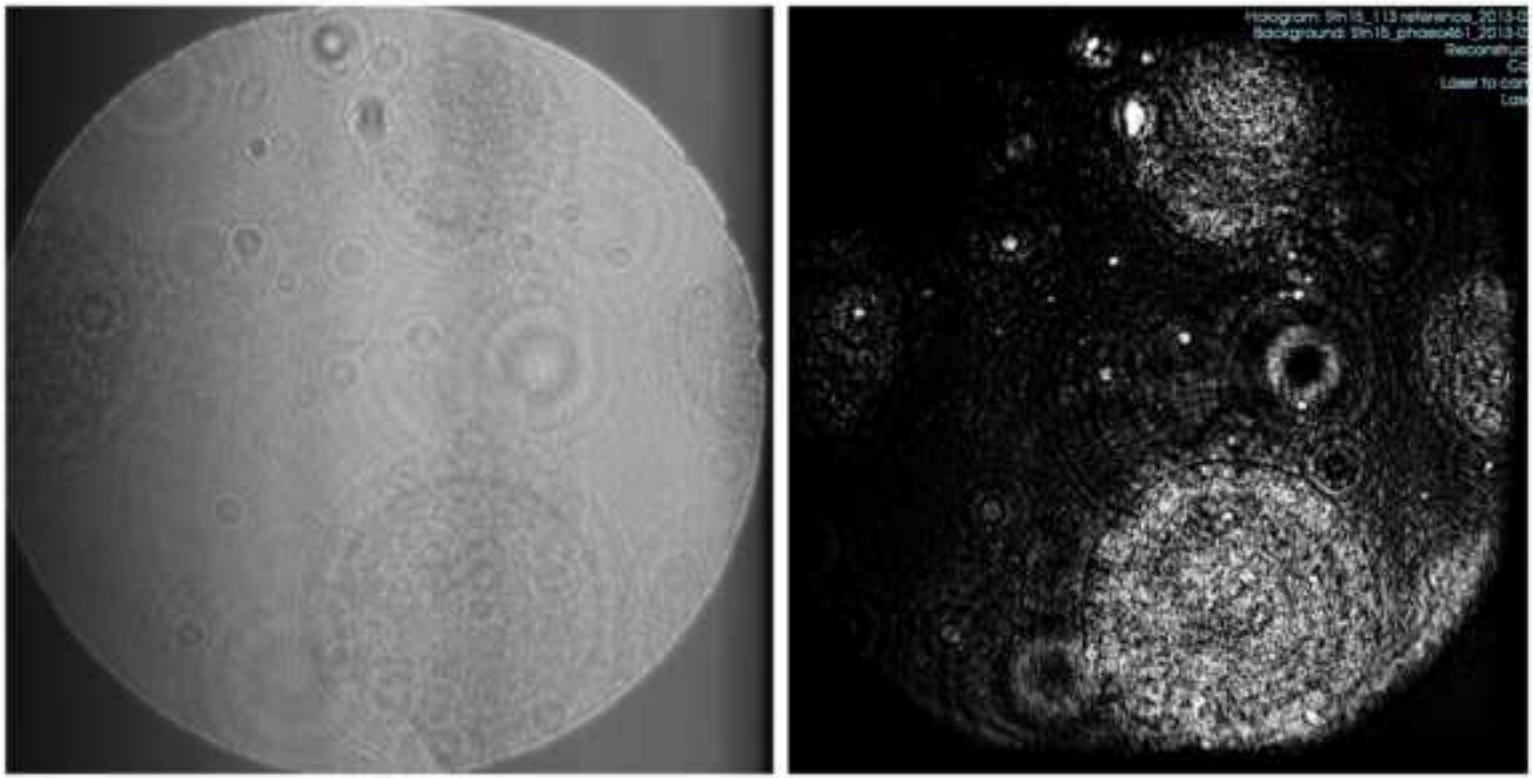

Fig. 3

Figure 4
Click here to download high resolution image

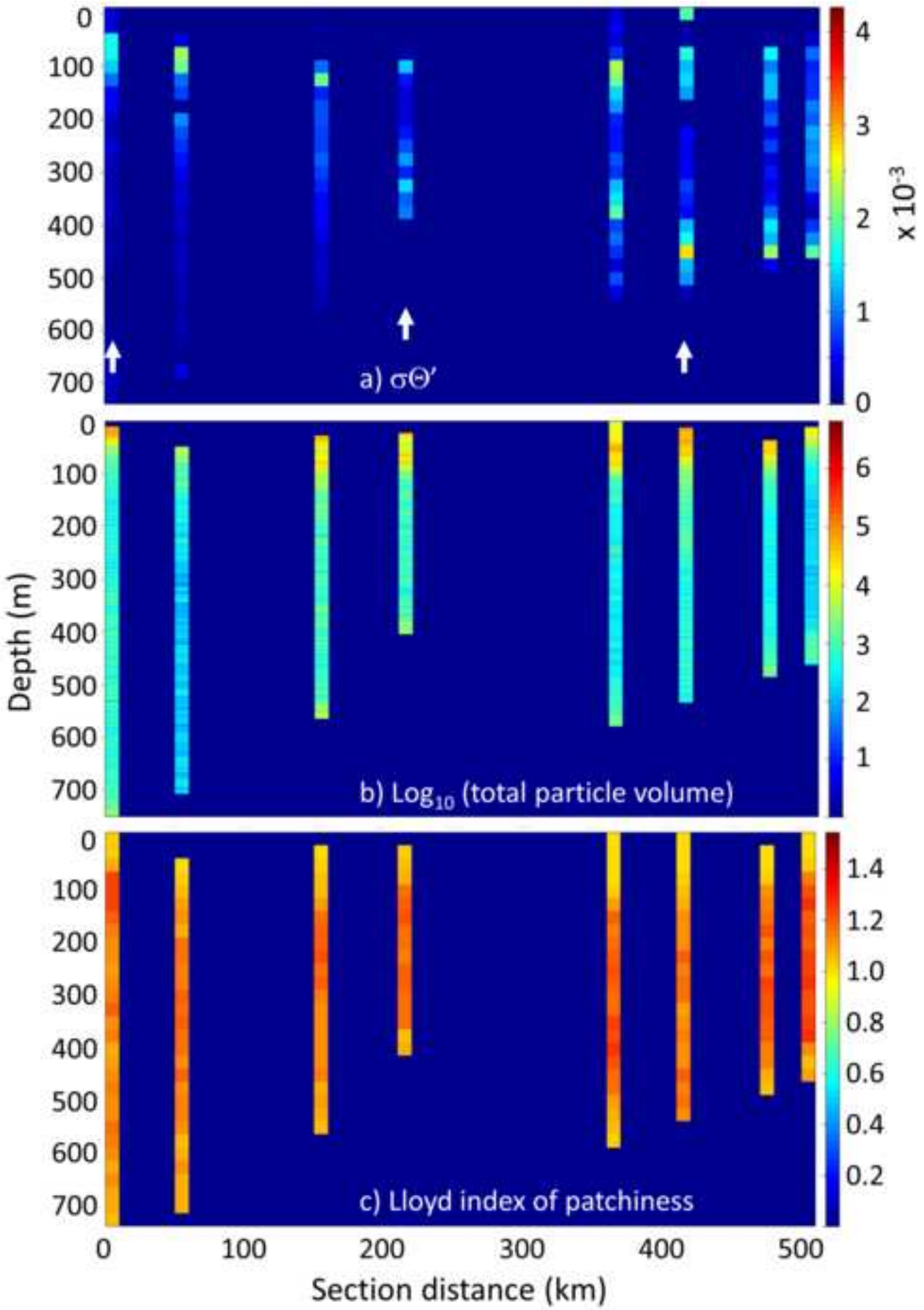

Fig. 4

Figure 5
Click here to download high resolution image

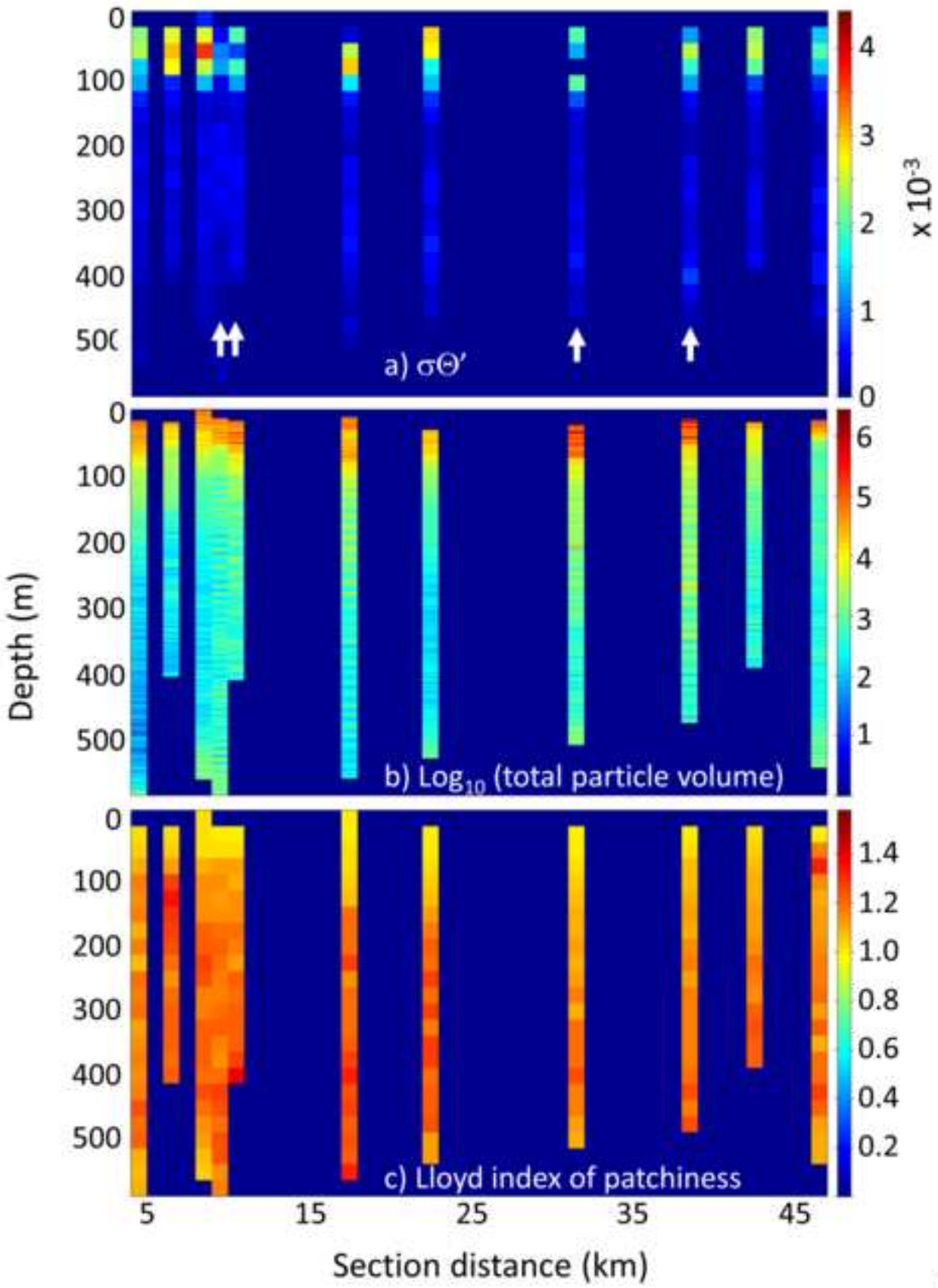

Fig. 5

Figure 6
Click here to download high resolution image

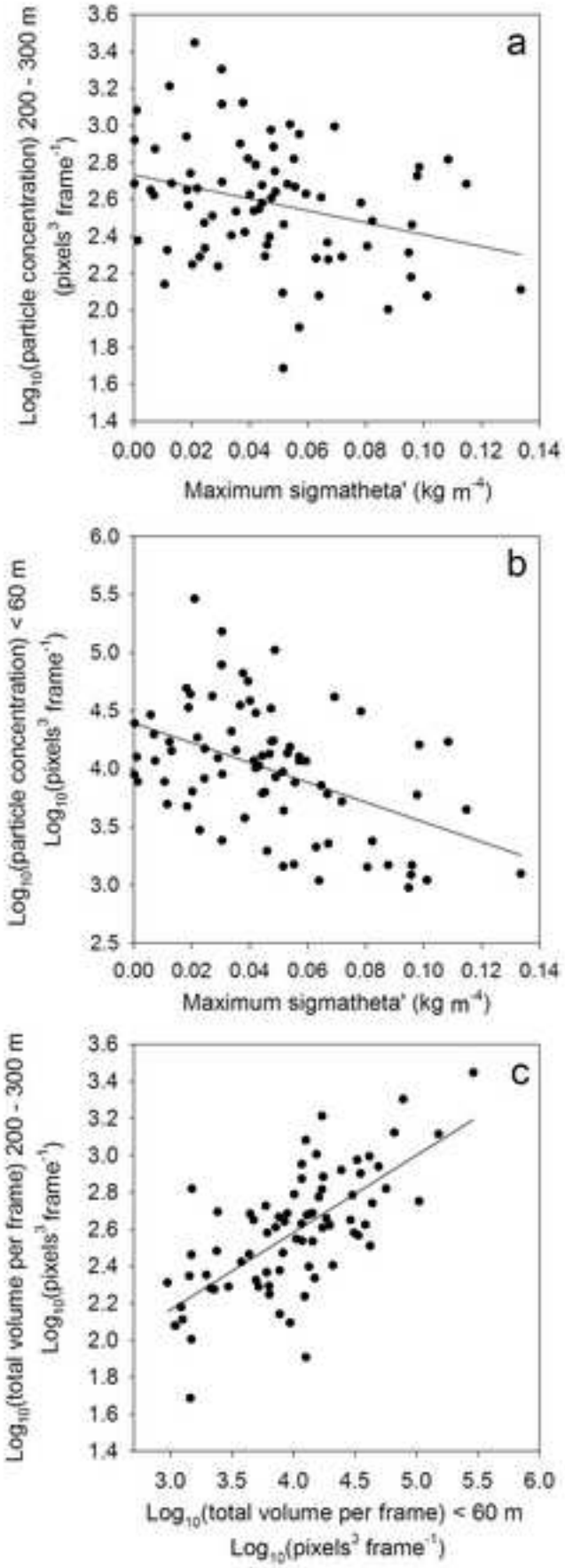

Fig. 6

Figure 7
Click here to download high resolution image

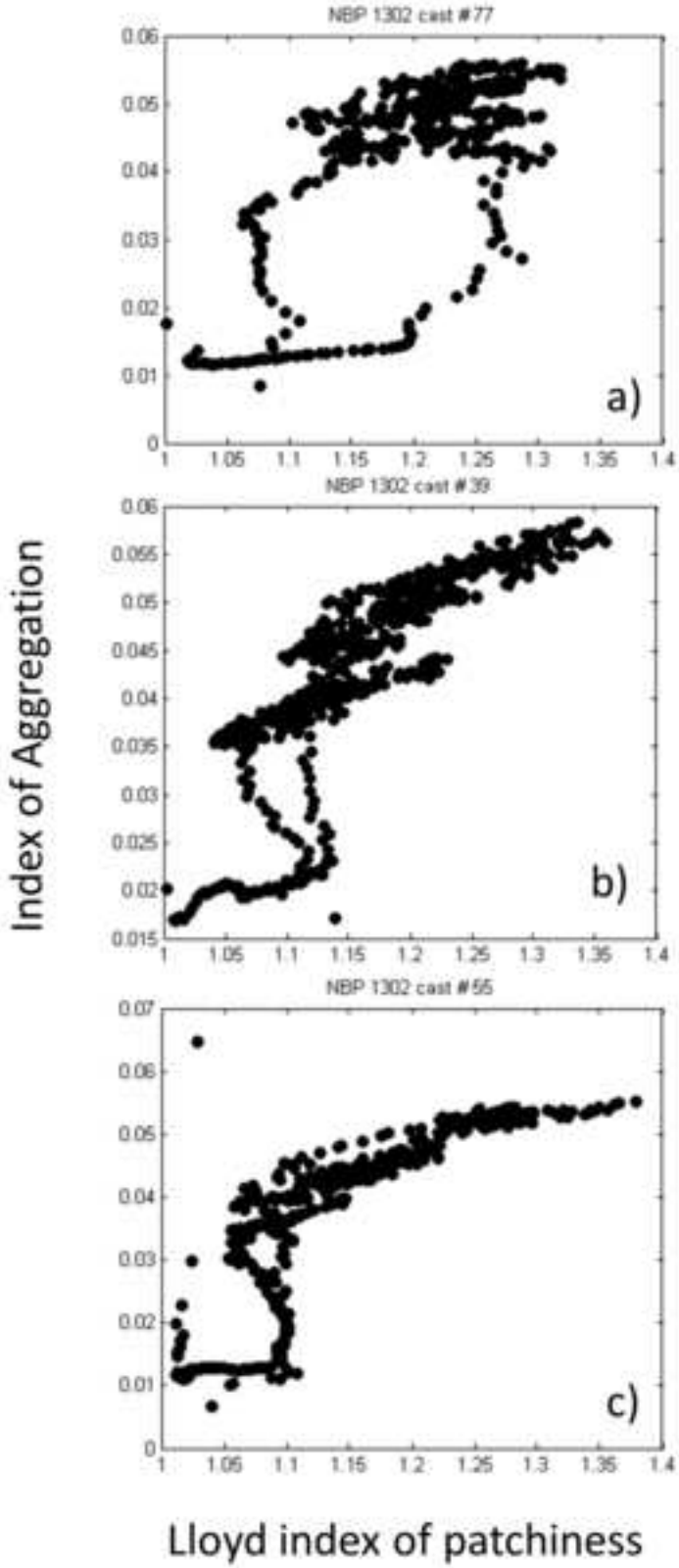

Fig. 7

Figure 8
Click here to download high resolution image

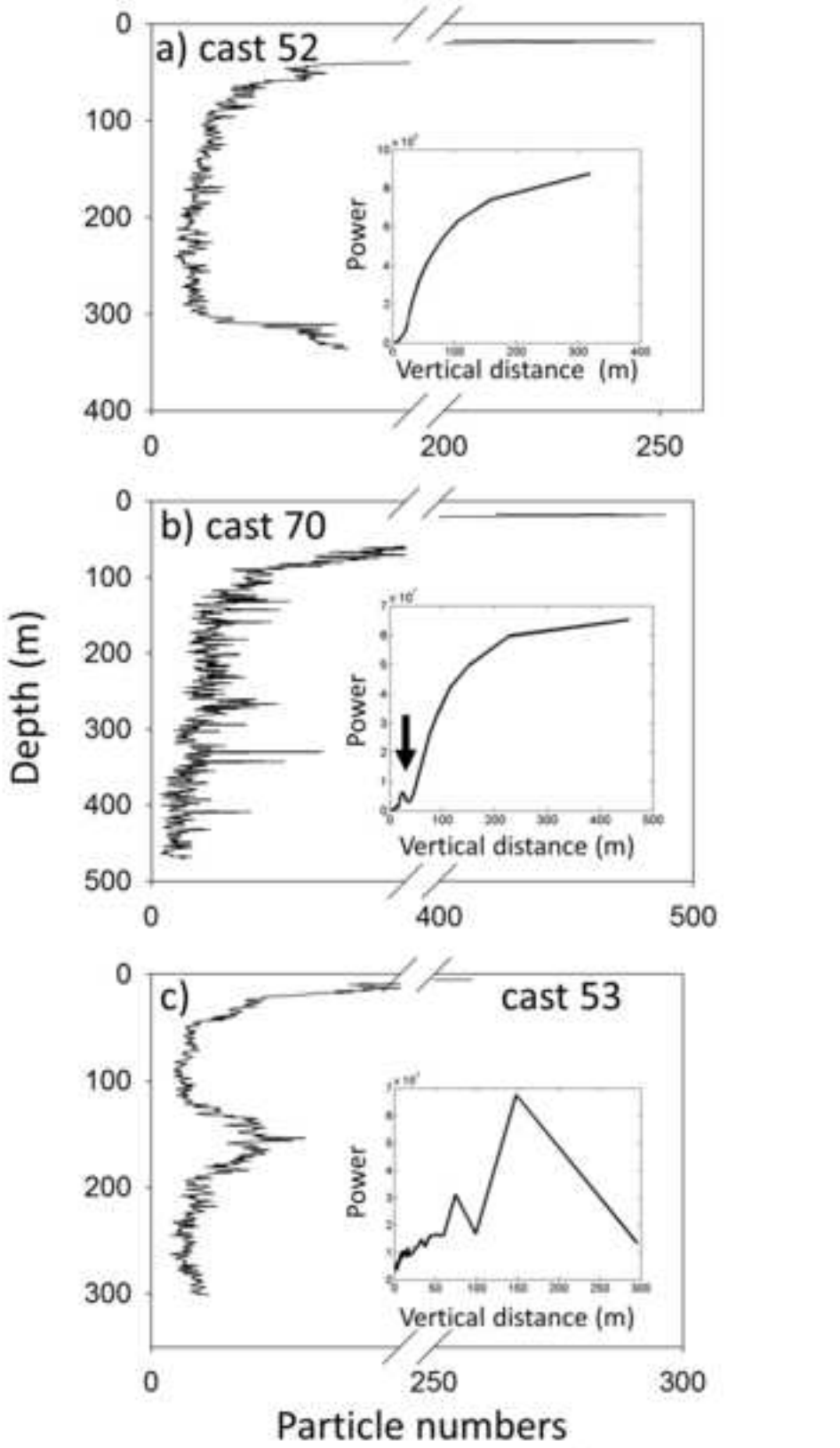

Fig. 8

Figure 9
Click here to download high resolution image

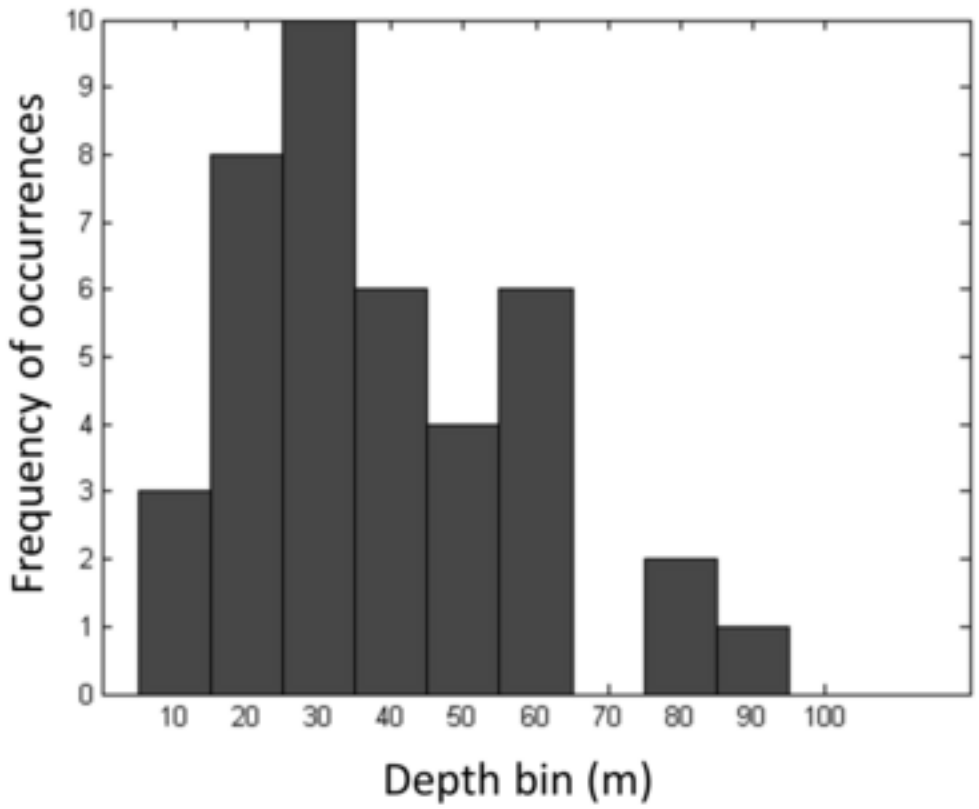

Fig. 9

Figure 10
Click here to download high resolution image

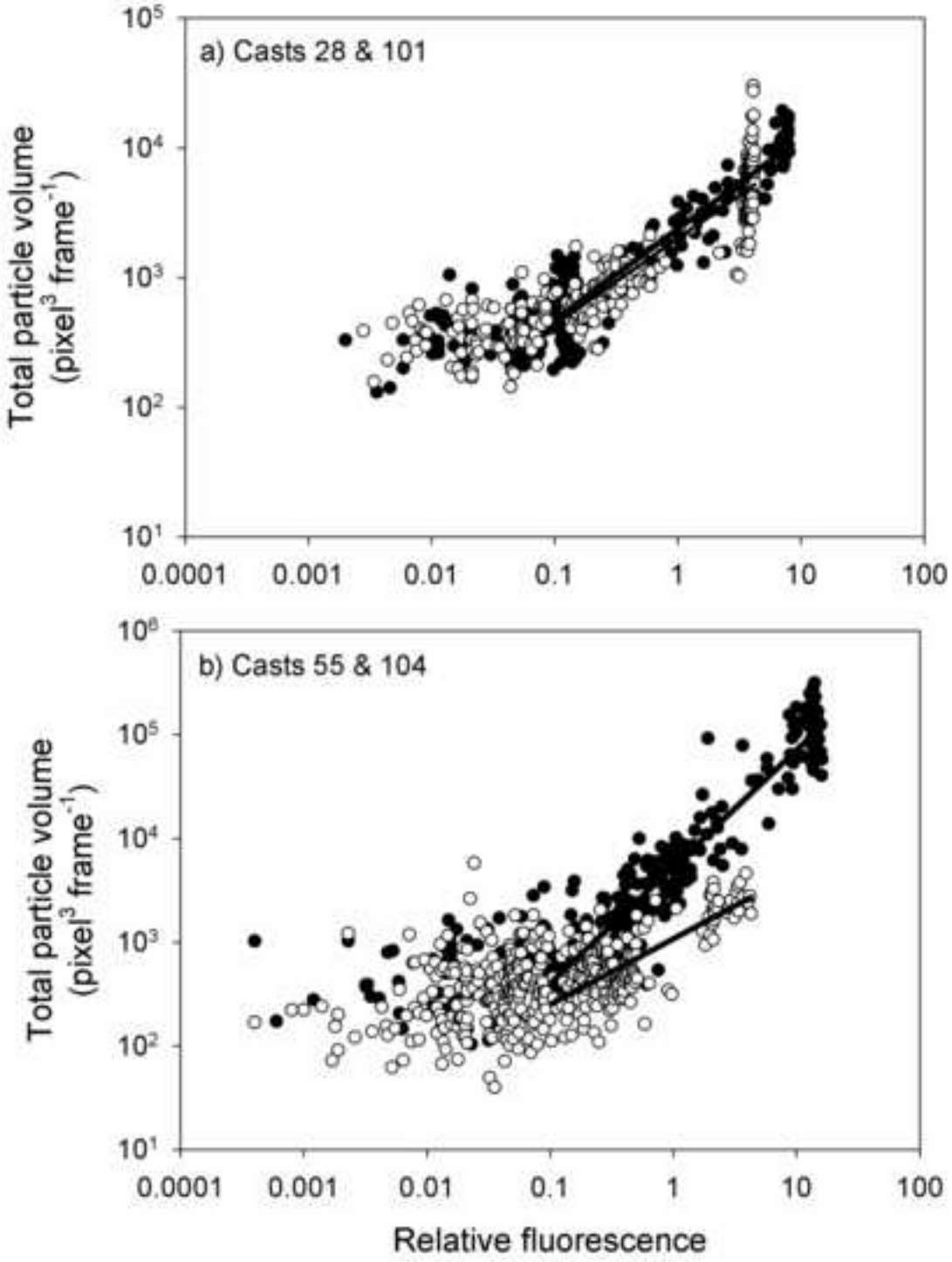

Fig. 10

Figure 11
Click here to download high resolution image

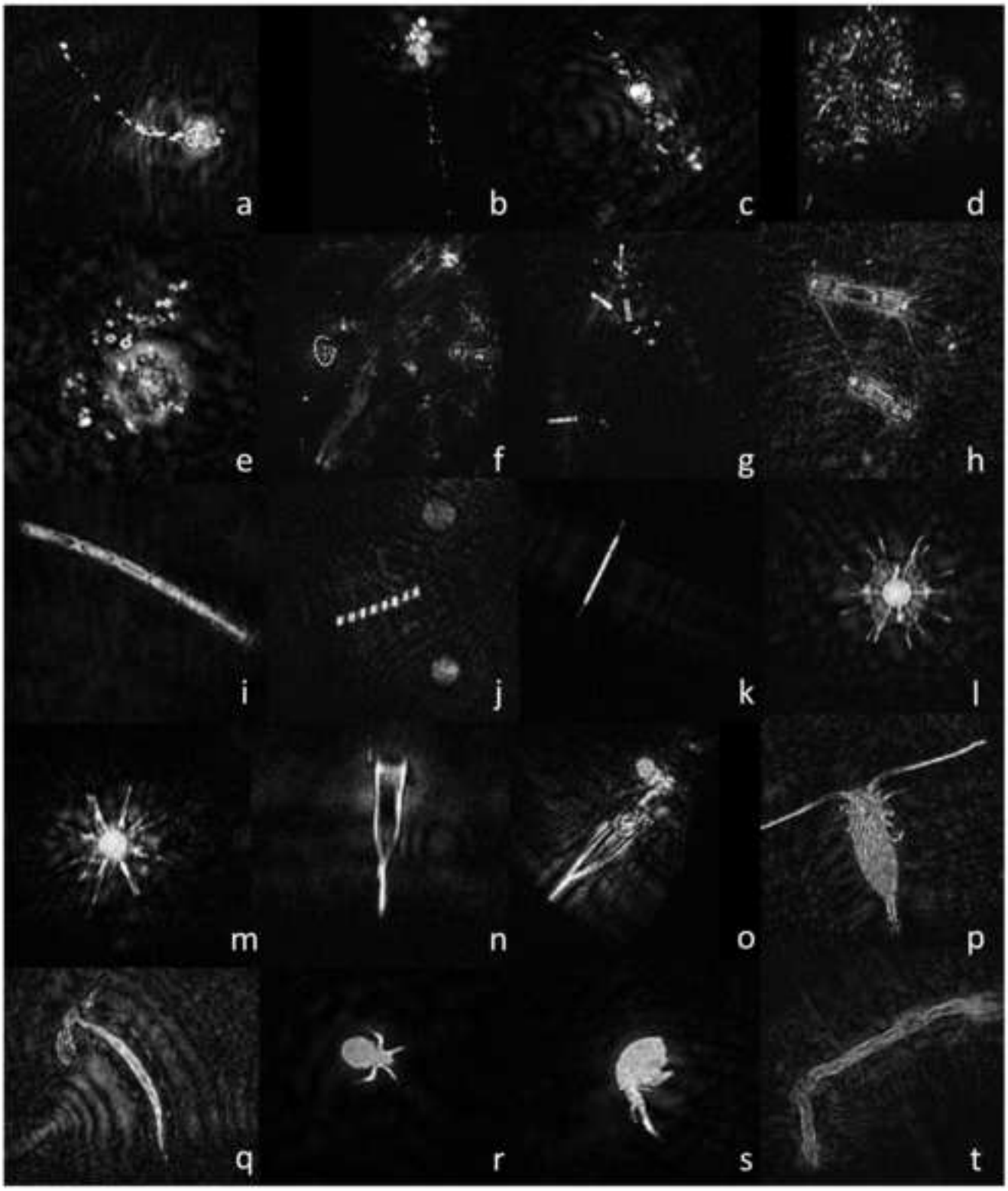

Fig. 11

Figure 12
Click here to download high resolution image

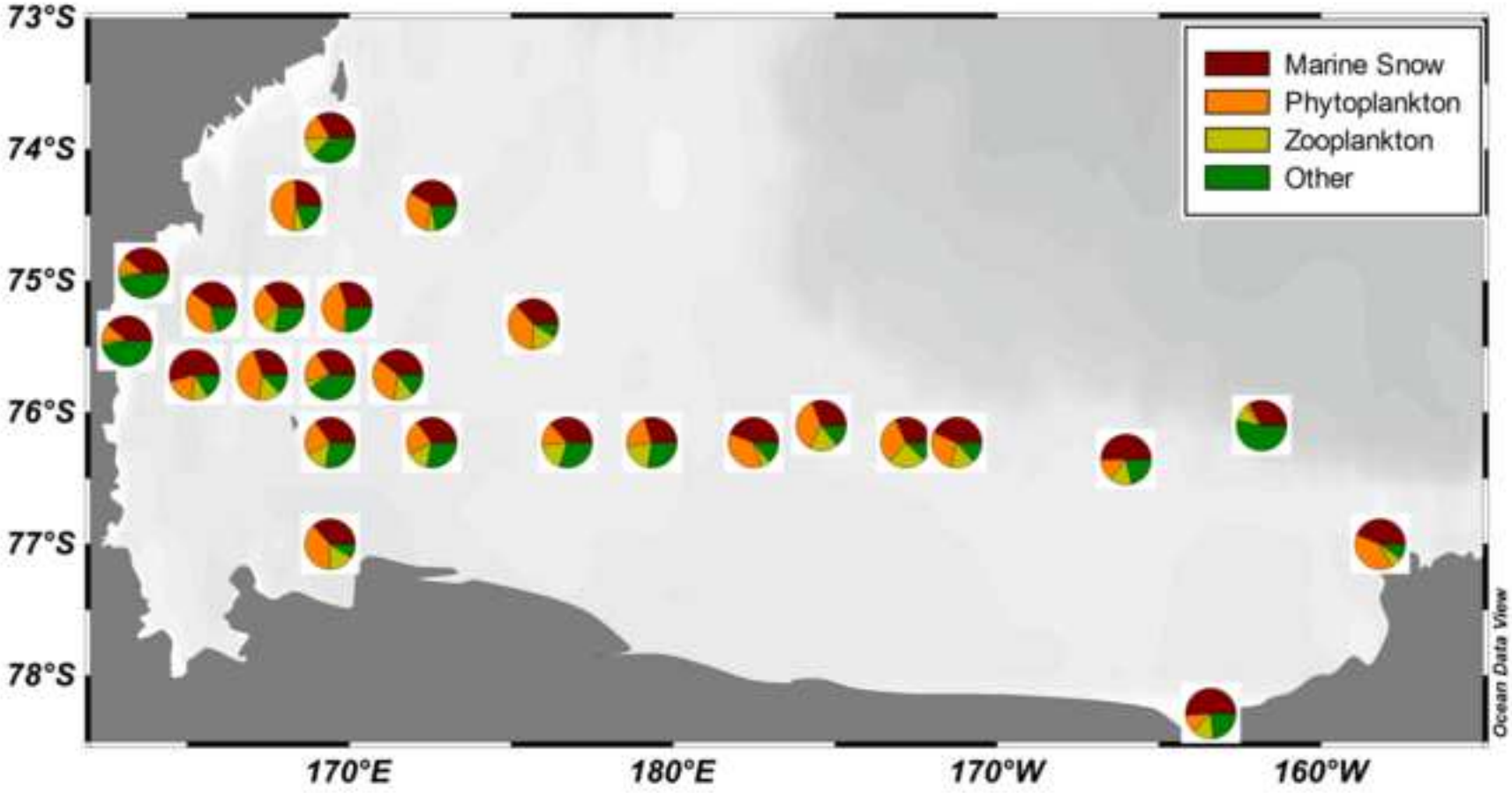

Fig. 12

Figure 13
Click here to download high resolution image

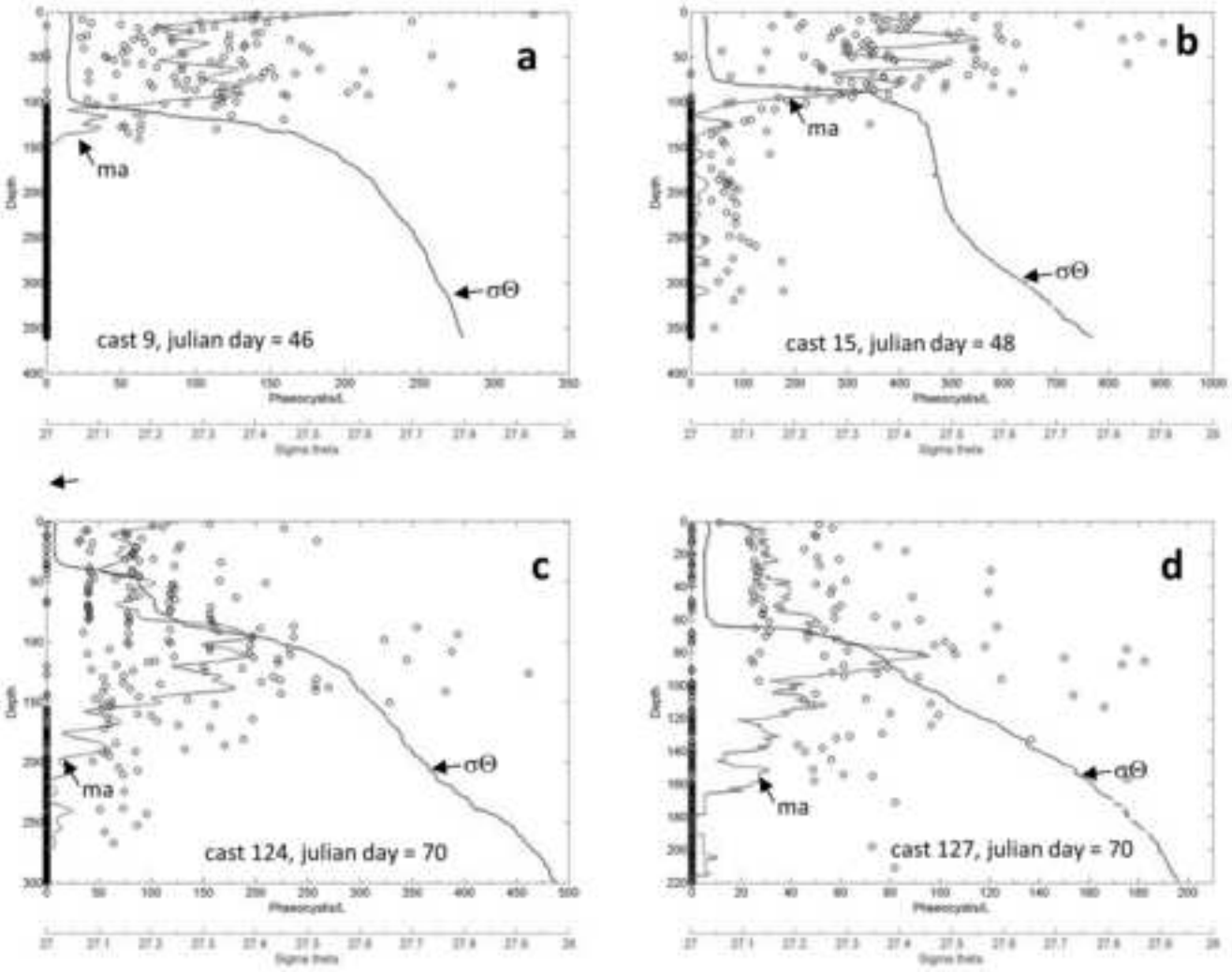

Fig. 13

Highlights:

- Particle profiles using a video plankton profiler and a digital inline holographic microscope
- Particle abundance at the surface is inversely related to the strength of the main pycnocline
- Particle abundance at depth is significantly correlated with that at the surface
- Phytoplankton and zooplankton comprise a large amount of exported particles
- The relationship between chlorophyll and particle abundance varies greatly